RESEARCH PAPER
*Contrib. Sci. & Tech Eng, 2024, 1(3)*
*Homepage: https://cste.journals.umz.ac.ir/*
*DOI: 10.22080/cste.2024.5111*

# Developing Modal Incremental Dynamic Analysis for Retrofitted Masonry Structures

**Zabih Mehdipour [1]*, Morteza Raissi Dehkordi [2]**

[1] *University of Minho, Guimarães, Portugal.*
[2] *Iran University of science and technology, Tehran, Iran.*

**Article Info**
Received 10 July 2024
Accepted 26 August 2024
Available online 1 September 2024

**Keywords:**
Masonry Structures;
MPA-Base IDA Technique;
Incremental Dynamic Analysis;
Retrofitting Implementations.

**Abstract:**

Given the inherently time-consuming nature of Incremental Dynamic Analysis (IDA), which requires extensive computational resources to simulate multiple ground motions and assess various structural responses, it is essential to explore more efficient methodologies that maintain accuracy while reducing analysis time. The MPA-based IDA algorithm (MIDA) is being developed for various structures to address the limitations of IDA. In this study, six individual masonry structures were examined, including three walls with varying perforation dimensions and three three-dimensional buildings subjected to two retrofitting conditions. These structures were analyzed using 30 ground motion accelerations. The masonry structures, reinforced with either a shotcrete layer or a coating application, were evaluated as homogeneous and anisotropic materials using a finite element-based macro-modeling approach. Additionally, IDA was performed, and the maximum displacement of the masonry structures was compared to that of the MIDA. The results indicate that, except under high surcharge conditions, the MIDA procedure not only significantly reduces computational time but also provides reasonable accuracy compared to the IDA precision algorithm. Therefore, it can be concluded that the difference between the IDA and MIDA methods is influenced by the lateral stiffness of the masonry structures being analyzed.



***Corresponding Author:** zabih.mehdipour@civil.uminho.pt

**Supplementary information:** Supplementary information for this article is available at https://cste.journals.umz.ac.ir/

**Please cite this paper as:** Mehdipour, Z., & Raissi Dehkordi, M. (2024). Developing Modal Incremental Dynamic Analysis for Retrofitted Masonry Structures. Contributions of Science and Technology for Engineering, 1(3), 10-24. doi: 10.22080/cste.2024.5111.

## 1. Introduction

To investigate structural behavior under seismic loading, several dynamic procedures have been proposed to assess damage measures in relation to intensity measurements. This study focuses on two methods applicable to masonry structures: the incremental dynamic analysis (IDA) method [1], which is the most accurate approach for determining the seismic behavior of structures, and the modal incremental dynamic analysis, which has been extended in the last two decades for various types of buildings, including steel and concrete structures. Notably, these algorithms ultimately produce a curve that describes the medium peak ground acceleration (PGA) of a series of scaled earthquakes, correlating it with various damage indices such as maximum roof displacement, maximum inter-story drift, maximum joint plastic rotation, and hysteretic energy of the structure [2].

The modal pushover algorithm was developed based on the similarities between rigorous linear response history analysis and standard response spectrum analysis in the linear range behavior of structures. This method aims to predict the inelastic response of structures with reasonably accurate results and significantly faster processing times compared to rigorous nonlinear response history analysis [3]. Subsequently, a new method was proposed that combines incremental dynamic analysis with modal pushover analysis (MPA) [4]. This approach achieves acceptable accuracy while dramatically reducing the time required compared to the IDA method. As a result, the MPA-based IDA algorithm (MIDA) has been enhanced for concrete structures, assuming a trilinear idealization of the pushover curve [5].

Using this MPA-based approximate procedure, curves similar to IDA curves—ranging from elastic behavior to global dynamic instability—have been generated [6]. Recently, the algorithm has been extended for structures controlled by viscoelastic dampers [7]. Additionally, the bilinear idealization of the pushover curve has been modified to obtain the hysteretic energy of a multi-degree-of-freedom system based on the structural hysteretic energy of an equivalent single-degree-of-freedom system [8]. The



*ISSN **3060-6578***

development of the MIDA technique has not only focused on 2D frames and 3D ordinary buildings but has also extended the modal pushover procedure to estimate the in-plane seismic responses of latticed arches [9].

In studies on masonry structures, various analytical strategies have been proposed based on factors such as structural dimensions and geometry, accuracy tolerance, loading conditions, analysis duration, and modeling expertise.

Replacing masonry walls with equivalent diagonal elements, commonly used in masonry-infilled frames, has been a subject of research for many years. The concept was first proposed to replace the infill in each panel with a diagonal element [10]. Subsequently, it was highlighted that the infill could be substituted with a pin-jointed diagonal strut made of the same material, provided that the thickness-to-diagonal length ratio of the strut is assumed to be one-third [11]. Based on various loading conditions and supported by experimental and analytical data, this ratio has been recommended as an analytical equation in numerous studies [12, 13]. Over the past three decades, it has been demonstrated that a single-strut element cannot adequately represent the behavior of masonry walls, a conclusion supported by extensive research [14-16].

Another method for modeling masonry walls, particularly those with openings, is the equivalent frame modeling strategy [17, 18]. This approach has been implemented using the TREMURI computer program [19].

Implementing the simplified modeling procedures mentioned earlier may lead to inaccurate responses, particularly under seismic loads, due to their inability to account for details such as material nonlinear behavior and structural interactions. Consequently, adopting a numerical approach becomes essential. In recent years, a significant number of masonry wall simulations have been conducted using finite element analysis. These numerical methods are categorized into three distinct approaches: micro-modeling, simplified micro-modeling, and macro-modeling, each aimed at assessing the performance of masonry walls [20, 21].

The most comprehensive evaluation method for masonry walls is micro-modeling. In this approach, all components, including units and mortar, are analyzed separately using continuum elements for the units and discontinuous elements for the unit/mortar interface [22]. However, this method is extremely time-consuming and is primarily recommended for the detailed study of small or historic structures. Due to the large memory requirements for processing and data storage, micro-modeling is not practical for other scenarios. Given these limitations, the simplified micro-modeling method is preferred, as it maintains accuracy without significant reductions in results. In this approach, larger units are represented using continuum elements, and the unit-mortar interface is approximated as a discontinuous element with mortar characteristics. Consequently, the masonry wall is treated as a composite material with elastic blocks and potential fracture lines at the joints [23].

In macro-modeling, the masonry wall is assumed to be an orthotropic homogeneous element, with material properties corresponding to the units and mortar. Tension and compression behaviors are treated differently based on the wall's properties in the head joint and bed joint directions [24]. The macro-modeling approach not only reduces analysis and modeling time but also simplifies mesh generation. In this study, the primary structure consists of solid walls of sufficient size. To avoid time-consuming analyses and modeling, the macro-modeling procedure is employed, despite an inevitable decrease in accuracy.

A substantial amount of research has been conducted on retrofitting existing unreinforced masonry buildings (URM) to enhance their strength under seismic loading and prevent sudden, catastrophic building collapses [25]. Surface treatments, particularly the application of shotcrete [26], stitching and grout/epoxy injection [27], repointing [28], and external reinforcement, including bamboo reinforcement [29] and glass fiber-reinforced polymer (GFRP) reinforcement [30], have been extensively explored. Additionally, strengthening the junctions of URM walls through L-shaped reinforcement and polypropylene (PP) bands [31], post-tensioning with rubber tires [32], confinement techniques [33], and various types of mesh reinforcement, such as polymer mesh reinforcement [34] and PP packaging strip mesh reinforcement [35, 36], along with coating applications for URM walls [37], represent some of the most significant rehabilitation strategies implemented across numerous countries. In the present work, we will focus on two specific interventions: shotcrete and coating for URM walls.

In this study, the MPA-Based IDA method will be applied to three 3D masonry buildings and three 2D masonry walls. The assessment of MIDA's efficiency will consider several significant parameters, including wall openings, story numbers, variations in surcharge, the impact of higher modes within the MIDA technique, and retrofitting methods using shotcrete and coating applications. Finally, the MIDA curves will be compared with the IDA curves. In all curves, the relationship between peak ground acceleration (PGA) and maximum displacement as a damage index will be illustrated.

## 2. Macro-modeling of Masonry Structures

Nonlinearity associated with an elastoplastic material simplifies the governing finite element equations to the following incremental form [38].

$$[K]\{\Delta u\}_i = \{\Delta f\}_i \quad (1)$$

where $[K]$ is the global system stiffness matrix, $\{\Delta u\}$ represents the vector of incremental nodal displacements, and $\{\Delta f\}$ denotes the vector of incremental nodal forces. Additionally, $i$ refers to the increment number. The global system stiffness matrix is derived by assembling the element stiffness matrices, which are defined by the following general formula:

$$[K^e] = \int_{-1}^{1}\int_{-1}^{1} B^T D B t |J| \, d\xi d\eta \quad (2)$$

In which D represents the elasticity matrix, which, in the case of plane stress, is defined by the following form:

$$[D] = \begin{bmatrix} \frac{E_x}{1-\nu_{xy}\nu_{yx}} & \frac{E_x\nu_{yx}}{1-\nu_{xy}\nu_{yx}} & 0 \\ \frac{E_y\nu_{xy}}{1-\nu_{xy}\nu_{yx}} & \frac{E_y}{1-\nu_{xy}\nu_{yx}} & 0 \\ 0 & 0 & G_{xy} \end{bmatrix} \quad (3)$$

where $E_x$ and $E_y$ are the moduli of elasticity, and $\nu_{xy}$ and $\nu_{yx}$ are Poisson's ratios for the x-direction (parallel to bed joints) and y-direction (parallel to head joints), respectively. Additionally, $B$ represents a suitable linear operator, determined for a four-node isoparametric rectangular finite element with 8 degrees of freedom, as shown in Figure 1, and is given by the following expression:

$$[B] = \begin{pmatrix} \frac{\partial N_1}{\partial x} & 0 & \frac{\partial N_2}{\partial x} & 0 & \frac{\partial N_3}{\partial x} & 0 & \frac{\partial N_4}{\partial x} & 0 \\ 0 & \frac{\partial N_1}{\partial y} & 0 & \frac{\partial N_2}{\partial y} & 0 & \frac{\partial N_3}{\partial y} & 0 & \frac{\partial N_4}{\partial y} \\ \frac{\partial N_1}{\partial y} & \frac{\partial N_1}{\partial x} & \frac{\partial N_2}{\partial y} & \frac{\partial N_2}{\partial x} & \frac{\partial N_3}{\partial y} & \frac{\partial N_3}{\partial x} & \frac{\partial N_4}{\partial y} & \frac{\partial N_4}{\partial x} \end{pmatrix} \quad (4)$$

which $N_1$, $N_2$, $N_3$ and $N_4$ represent the shape functions at nodes 1 through 4, respectively, are obtained as follows:

$$\begin{aligned} N_1 &= \tfrac{(1-\xi)(1-\eta)}{4} \\ N_2 &= \tfrac{(1+\xi)(1-\eta)}{4} \\ N_3 &= \tfrac{(1+\xi)(1+\eta)}{4} \\ N_4 &= \tfrac{(1-\xi)(1+\eta)}{4} \end{aligned} \quad (5)$$

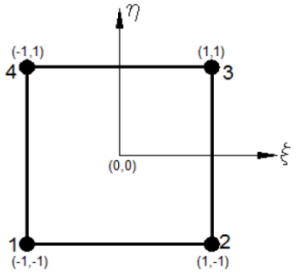


**Figure 1. The rectangular element**

In the preceding equation, $\xi$ and $\eta$ are the natural coordinates of the four-node rectangular elements (shown in Figure 1). Additionally, $t$ is the thickness of the masonry wall, and $|J|$ denotes the determinant of the Jacobian matrix, which relates the derivatives of the shape functions in local coordinates, as follows:

$$[J] = \begin{bmatrix} \frac{\partial N_1}{\partial \xi} & \frac{\partial N_2}{\partial \xi} & \frac{\partial N_3}{\partial \xi} & \frac{\partial N_4}{\partial \xi} \\ \frac{\partial N_1}{\partial \eta} & \frac{\partial N_2}{\partial \eta} & \frac{\partial N_3}{\partial \eta} & \frac{\partial N_4}{\partial \eta} \end{bmatrix} \begin{bmatrix} \Delta x_1 & \Delta y_1 \\ \Delta x_2 & \Delta y_2 \\ \Delta x_3 & \Delta y_3 \\ \Delta x_4 & \Delta y_4 \end{bmatrix} \quad (6)$$

In this equation, $(\Delta x_1, \Delta y_1)$ to $(\Delta x_4, \Delta y_4)$ represent the incremental nodal displacements at joints 1 to 4 in the global coordinate system.

During the evaluation of the stiffness matrix, integration over the element's area is required. Numerical integration is crucial for accurately evaluating these integrals within the element's domain. The conventional method for this is the Gauss integration formula, as it utilizes the minimum number of sample points to achieve the desired accuracy. After assembling the incremental nodal displacements and forces in the global system and solving for $\{\Delta u\}_i$, the incremental strain is determined by:

$$\{\Delta\varepsilon\}_i = [B]\{\Delta u\}_i \quad (7)$$

It is important to note that if the material is yielding, the strains will consist of both elastic and plastic components. Additionally, according to Hooke's law, the equilibrium between stress and strain is expressed as follows:

$$\{\Delta\sigma\}_i = [D]\{\Delta\varepsilon\}_i \quad (8)$$

These stresses are subsequently added to the previously accumulated stresses as shown in the following formula. The resulting stresses are then checked to determine whether yield has been violated [39].

$$\sigma_i = \sigma_{i-1} + \{\Delta\sigma\}_i \quad (9)$$

The masonry failure surface is recalculated using this stress. If the failure surface is below zero ($f(\sigma) < 0$), the material remains in the elastic state, and the process is repeated with an increased load ($i = i + 1$) in Equation 1. However, if the failure surface exceeds zero ($f(\sigma) > 0$), the stress is overestimated and must be redistributed to bring it back as close as possible to the yield surface ($f(\sigma) = 0$). At this point, the material behaves plastically, and the plastic strains must be calculated.

Finally, using the return mapping algorithm [21], the following set of four consecutive equations with four unknowns (the $\sigma_i$ components and $\Delta\lambda$ representing the increment of the plastic multiplier) must be solved:

$$\begin{cases} F = D^{-1}(\sigma_i - \sigma^{trial}) + \Delta\lambda\frac{\partial f}{\partial \sigma} = 0 \\ f(\sigma_i) = 0 \end{cases} \quad (10)$$

which $\sigma^{trial}$ is obtained in the following manner:

$$\sigma^{trial} = \sigma_{i-1} + D\{\Delta\varepsilon\}_i \quad (11)$$

The set of equations mentioned above should be solved using the Newton-Raphson method, which is extended for a nonlinear system of equations. Therefore, the equations are rewritten in the following iterative form, assuming $\sigma_i = \sigma^{trial}$ and $\Delta\lambda = 0$ as the starting point:

$$\begin{bmatrix} \sigma_i \\ \Delta\lambda \end{bmatrix}^{j+1} = \begin{bmatrix} \sigma_i \\ \Delta\lambda \end{bmatrix}^{j} - J^{-1}\begin{bmatrix} F \\ f \end{bmatrix} \quad (12)$$

Here, $j$ represents the iteration of the solving procedure. The $J$, known as the Jacobian matrix, is defined as follows:

$$[J] = \begin{pmatrix} \frac{\partial F}{\partial \sigma} & \frac{\partial F}{\partial \Delta\lambda} \\ \frac{\partial f}{\partial \sigma} & 0 \end{pmatrix} \quad (13)$$

The modified elastic matrix is governed by the following equation:

$$D_{Modified} = (J^{-1})_{3x3} \quad (14)$$

where $(J^{-1})_{n_\sigma * n_q}$ is the top-left 3x3 submatrix of the inverse of the Jacobian $J$. During the iteration process outlined in Equation 12, the operation is repeated until the stresses are sufficiently close to the yield surface within a specified error, which should be less than a predefined tolerance typically set to 0.01. Once this criterion is met, the solution is considered converged. The entire procedure explained so far is illustrated in Figure 2.

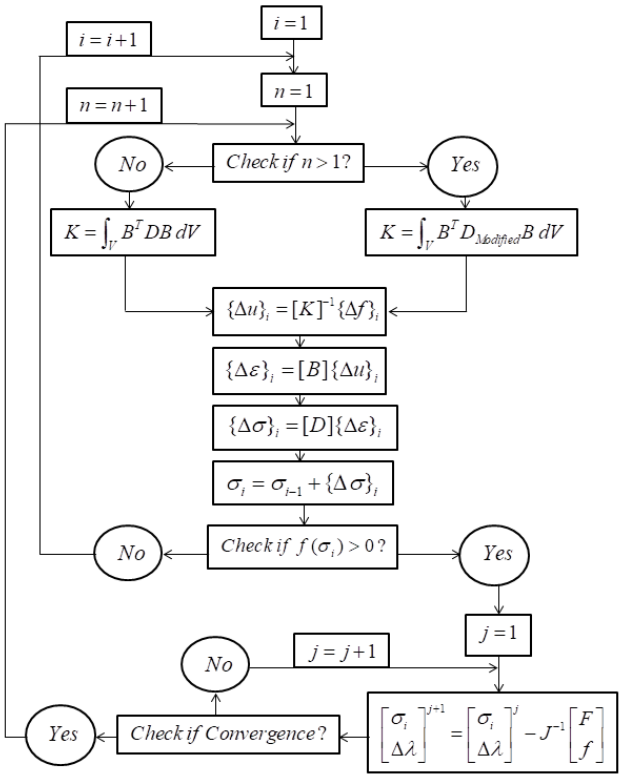


**Figure 2. Elasto-plastic algorithm for an anisotropic continuum masonry model**

## 3. Review of the MPA-Based IDA Method

For implementing the MPA-based IDA technique, the following steps will be briefly considered [3]:

- Modelling and design of the structure
- Evaluating the first few dominant modes of the structure and the participation factor of each mode
- Applying forces to the structure that are proportional to mass inertia, expressed as $s = m\varphi$ for each mode
- Equating the pushover curve to the generated bilinear curve to extract the yield strength $F_y$ and the strain hardening angle $\alpha$ of the material.
- Converting the MDOF bilinear curve to the SDOF bilinear curve using the relationships illustrated in Figure 3.

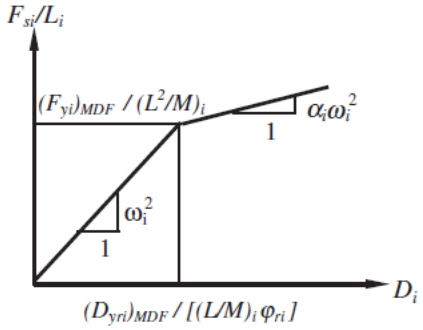


**Figure 3. SDOF Bilinear curve**

$$\begin{aligned} (F_{yi})_{SDF} &= (F_{yi})_{MDF}/(L/M)_i \\ (U_{riy})_{SDF} &= (U_{riy})_{MDF}/(L/M)_i\phi_{ri} \\ \alpha_{SDF} &= \alpha_{MDF} \\ L_i &= \sum m_j\phi_{ji}\ M_i = \sum m_j{\phi_{ji}}^2 \end{aligned} \quad (15)$$

In this context, $\varphi_{ri}$ represents the roof mode shape for mode $i$ and $\alpha$ denotes the strain hardening angle of the material. Additionally, $F_y$ signifies the yielding stress. Furthermore, $U_{riy}$, $L_i$, and $M_i$ represent the roof yielding displacement, a modal coefficient, and modal mass for mode $i$, respectively.

- Preparing the group acceleration records and scaling them in relation to the distinguished PGA after applying significant corrections, such as baseline modification and filtering.
- Applying the scaled records to the SDOF system, performing the nonlinear time history analysis, and computing the maximum displacement of the SDOF structure.
- Transforming the maximum displacement of the SDOF system to the principal MDOF structure based on the following equation:

$$Dis_{Max,MDOF} = (L/M)_i.\Phi_{ri}.Dis_{Max,SDOF} \quad (16)$$

where $Dis_{Max,MDOF}$ and $Dis_{Max.SDOF}$ represent the maximum displacements of the MDOF and SDOF structures, respectively.

- Applying a lateral load to the main MDOF structure until reaching the maximum displacement calculated in the previous step, and then determining the maximum drift as a damage index.
- Summing all maximum drifts of the MDOF system obtained for the first few predominant modes of the structure using the Square Root of the Sum of Squares (SRSS) method.

## 4. Extending the MPA-based IDA Technique To Masonry Structures

### 4.1. Earthquakes records

To analyse different masonry structures, thirty records were selected. All records correspond to soil groups C and D, according to ASCE/SEI 7-16 [40]. The magnitudes of the records range from 6.0 to 7.0, and the distance to the fault lies between 20 km and 40 km. Additionally, no near-fault

motions with directivity effects were included. The characteristics of all records are provided in Table 1.

### 4.2. The geometry of Masonry Structures

The following section outlines all structures used for the subsequent analyses, including three 2D walls and three 3D buildings. The 2D walls (shown in Figure 4) measure 2 m in width, 3 m in height, and 0.2 m in thickness. Three types of walls will be analyzed: one without holes, one with a 0.5x0.5 m² hole at the center, and one with a 1×1 m² hole at the center. To assess the effect of surcharge, a beam measuring 0.2 m in width, 0.1 m in height, and 2 m in length will be placed on top of the walls. The one-story 3D building (shown in Figure 5), designed without retrofitting, has dimensions of 12.5 m in length, 8 m in width, and 3 m in height, with an internal wall thickness of 0.11 m and an external wall thickness of 0.3 m. All windows measure 1 m by 1 m, and all doors measure 1 m by 2 m. The building features a concrete slab on top of the walls, which has a thickness of 0.2 m. Additionally, a two-story and a three-story masonry building, identical in geometry and materials to the one-story building, are included to examine the influence of the number of stories.

As previously mentioned, all three 3D buildings - one-story, two-story, and three-story - have been retrofitted using shotcrete and coating applications. In the former method, a reinforcement mesh with a diameter of 8 mm and a spacing of 150 mm is installed around the external walls, extending the full height of all buildings, embedded within a 5 cm concrete layer. In the latter method, concrete walls are constructed at the four corners of the external walls, extending 3 m in both horizontal orthogonal directions and covering the full height of all buildings. To reinforce these concrete walls, two reinforcement meshes with a diameter of 12 mm and a spacing of 150 mm are used.

**Table 1. 30 earthquake records characteristics**

| No. | Earthquake Name | Year | Station Name | Magnitude | Distance (km) | Vs30 (m/sec) |
|---|---|---|---|---|---|---|
| 1 | Imperial Valley-06 | 1979 | Superstition Mtn Camera | 6.53 | 24.61 | 362.38 (D) |
| 2 | Imperial Valley-06 | 1979 | Victoria | 6.53 | 31.92 | 242.05 (D) |
| 3 | Imperial Valley-06 | 1979 | El Centro Array #13 | 6.53 | 21.98 | 249.92 (D) |
| 4 | Victoria_ Mexico | 1980 | SAHOP Casa Flores | 6.33 | 39.1 | 259.59 (D) |
| 5 | Irpinia_ Italy-01 | 1980 | Rionero In Vulture | 6.9 | 27.49 | 574.88 (C) |
| 6 | Irpinia_ Italy-01 | 1980 | Bisaccia | 6.9 | 21.26 | 496.46 (C) |
| 7 | Irpinia_ Italy-02 | 1980 | Sturno (STN) | 6.2 | 20.39 | 382 (C) |
| 8 | Coalinga-01 | 1983 | Parkfield - Fault Zone 12 | 6.36 | 27.96 | 265.21 (D) |
| 9 | Coalinga-01 | 1983 | Parkfield - Gold Hill 2E | 6.36 | 31.85 | 360.92 (D) |
| 10 | Coalinga-01 | 1983 | Parkfield - Vineyard Cany 1E | 6.36 | 24.83 | 381.27 (C) |
| 11 | Friuli_ Italy-01 | 1976 | Codroipo | 6.5 | 33.4 | 249.28 (D) |
| 12 | Superstition Hills-02 | 1987 | Plaster City | 6.54 | 22.25 | 316.64 (D) |
| 13 | Superstition Hills-02 | 1987 | Calipatria Fire Station | 6.54 | 27 | 205.78 (D) |
| 14 | Spitak_ Armenia | 1988 | Gukasian | 6.77 | 23.99 | 343.53 (D) |
| 15 | Loma Prieta | 1989 | Calaveras Reservoir | 6.93 | 35.49 | 571.99 (C) |
| 16 | Loma Prieta | 1989 | Palo Alto - SLAC Lab | 6.93 | 30.86 | 425.3(C) |
| 17 | Loma Prieta | 1989 | Halls Valley | 6.93 | 30.49 | 281.61 (D) |
| 18 | Northern Calif-03 | 1954 | Ferndale City Hall | 6.5 | 27.02 | 219.31 (D) |
| 19 | Griva_ Greece | 1990 | Edessa (bsmt) | 6.1 | 33.29 | 551.3 (C) |
| 20 | Griva_ Greece | 1990 | Kilkis | 6.1 | 29.2 | 454.56 (C) |
| 21 | San Fernando | 1971 | LA - Hollywood Stor FF | 6.61 | 22.77 | 316.46 (D) |
| 22 | San Fernando | 1971 | Pasadena - CIT Athenaeum | 6.61 | 25.47 | 415.13 (C) |
| 23 | Morgan Hill | 1984 | Capitola | 6.19 | 39.08 | 288.62 (D) |
| 24 | Morgan Hill | 1984 | Corralitos | 6.19 | 23.23 | 462.24 (C) |
| 25 | Morgan Hill | 1984 | San Juan Bautista_ 24 Polk St | 6.19 | 27.15 | 335.5 (D) |
| 26 | N. Palm Springs | 1986 | Indio | 6.06 | 35.34 | 307.54 (D) |
| 27 | N. Palm Springs | 1986 | Joshua Tree | 6.06 | 23.2 | 379.32 (C) |
| 28 | Chalfant Valley-02 | 1986 | Benton | 6.19 | 21.55 | 370.94 (C) |
| 29 | Chalfant Valley-02 | 1986 | Convict Creek | 6.19 | 29.35 | 382.12 (C) |
| 30 | Chalfant Valley-02 | 1986 | Mammoth Lakes Sheriff Subst. | 6.19 | 34.92 | 529.39 (C) |

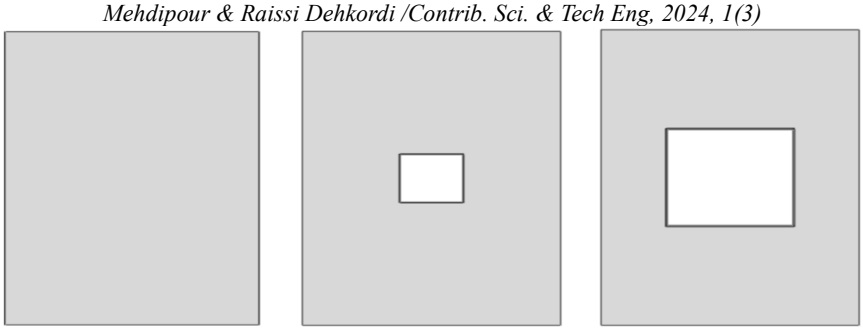

(a) (b) (c)

**Figure 4: Masonry walls, (a) a 2×3 $m^2$ wall without a hole, (b) a 2×3 $m^2$ wall with hole 0.5x0.5 $m^2$ at center, (c) a 2×3 $m^2$ wall with hole 1x1 $m^2$ at center**

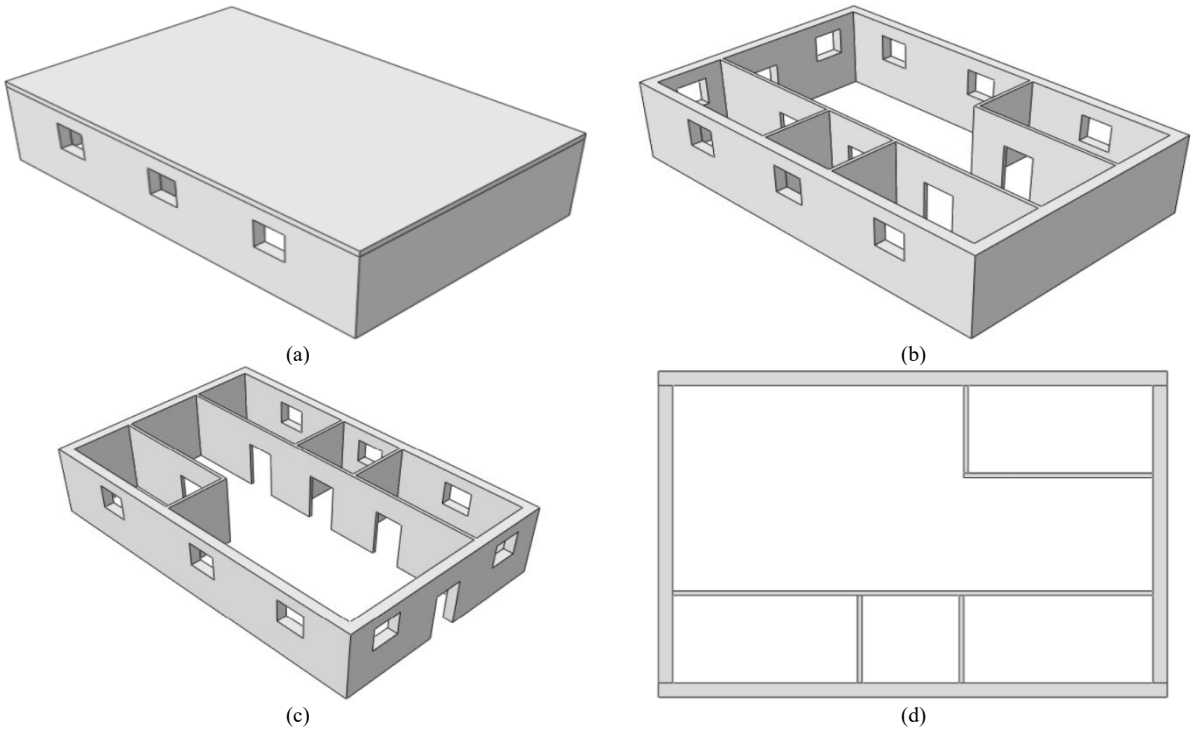

(a) (b) (c) (d)

**Figure 5: The 3D masonry building, (a) 3D view with roof, (b) 3D view without the roof, (c) 3D view without the roof (Another view), (d) Plan**

### 4.3. Material Properties

The Kent and Park model [41], shown in Figure 6, is employed for both the confined and unconfined concrete constitutive models.

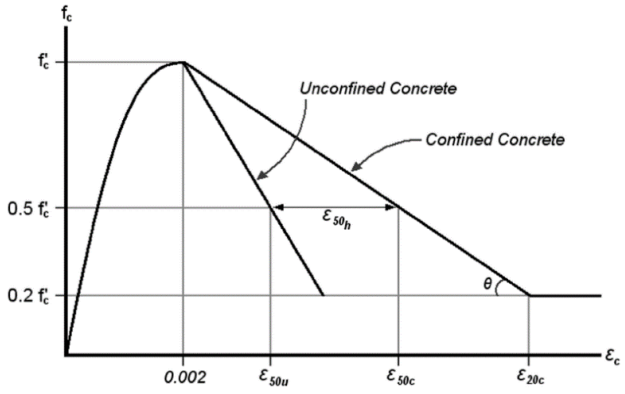


**Figure 6. Concrete constitutive model [41]**

In the preceding figure, $f'_c$ represents the peak compressive strength of concrete. The terms $\varepsilon_{50u}$ , $\varepsilon_{50c}$ , $\varepsilon_{20c}$ denote the strains corresponding to $0.5f'_c$ for unconfined concrete, $0.5f'_c$ for confined concrete, and $0.2f'_c$ for confined concrete, respectively.

In the current study, the masonry failure surface is defined by the equation $f(\sigma) = 0$ representing a general anisotropic failure under biaxial stress (plane stress) as given in the following equation [42]:

$$2.27\sigma_x + 9.87\sigma_y + 0.573{\sigma_x}^2 + 1.32{\sigma_y}^2 + 6.25\tau^2 - 0.3\sigma_x\sigma_y + 0.009585{\sigma_x}^2\sigma_y + 0.003135\sigma_x{\sigma_y}^2 + 0.28398\sigma_x\tau^2 + 0.4689\sigma_y\tau^2 - 1 = 0 \quad (17)$$

Here, $\sigma_x$, $\sigma_y$ and $\tau$ represent the stresses in the x-direction, y-direction, and shear stress, respectively. The elastic properties of concrete and masonry in the two orthogonal directions are provided in Table 2 [43]

**Table 2.** Concrete and masonry elastic properties

| Material | Moduli of elasticity | | Posion's ratio | | Density |
|---|---|---|---|---|---|
| | $E_x\ (KN/m^2)$ | $E_y\ (KN/m^2)$ | $\nu_{xy}$ | $\nu_{yx}$ | $\rho\ (Kg/m^3)$ |
| Concrete | 2.9e7 | 2.9e7 | 0.2 | 0.2 | 2400 |
| Concrete masonry | 4.5e6 | 7.5e6 | 0.19 | 0.32 | 1800 |

It should be noted that in the case of plane stress in an anisotropic material, the following equation supports this [44]:

$$E_x \nu_{yx} = E_y \nu_{xy} \tag{18}$$

To obtain the peak compressive strength of concrete, the following empirical relationship is prescribed [45]:

$$E = 0.043 \rho^{1.5} \sqrt{f'_c} \tag{19}$$

This formula is valid for values of $\rho$between 1440 and 2560 kg/m³. For modeling the reinforcement, a bilinear elastic-plastic constitutive model is established as follows (Figure 7):

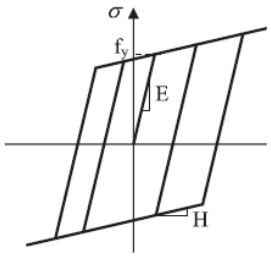


**Figure 7.** Steel constitutive model

In the above figure, $f_y$ represents the yield stress of steel. Additionally, $E$ and $H$ denote the modulus of elasticity and the modulus of plasticity of steel, respectively. The strain corresponding to the stress $f_y$ is represented as $\varepsilon_y$. Furthermore, the elastic and plastic properties of the reinforcement are detailed in Table 3.

**Table 3:** Elasto-Plastic properties of reinforcement

| Density | Moduli of elasticity | Posion's ratio |
|---|---|---|
| $\rho\ (Kg/m^3)$ | $E\ (GPa)$ | $\nu$ |
| 7850 | 210 | 0.3 |
| **Yield stress** | **Moduli of plasticity** | **Yield strain** |
| $f_y\ (MPa)$ | $H\ (GPa)$ | $\varepsilon_y$ |
| 420 | 6.3 | 0.0021 |

### 4.4. Conducting the IDA and MPA-based IDA Algorithms on the Masonry Structures

All analyses presented compare the efficiency of the proposed algorithm, MPA-based IDA, to the exact method, IDA. To achieve a comprehensive evaluation, several parameters that may significantly affect masonry structures are briefly outlined below.

a. Various types of masonry structures to account for in-plane and out-of-plane performance effects

b. Number of stories in the 3D masonry buildings to evaluate the effects of higher modes in the MPA technique

c. Whether the 3D buildings have been retrofitted. In other words, whether strengthening enhances or disrupts the MPA technique in relation to the IDA algorithm

d. The degree of nonlinearity in the masonry material during the pushover analysis of the main structure in the MPA procedure or while conducting the IDA technique. Failure occurs when the maximum stress exceeds the allowable stress, defined as the stresses encountered on the masonry failure surface multiplied by a fixed coefficient. In this study, coefficients of 1 and 10 are used to represent low and high nonlinearity levels, respectively. To further investigate the masonry behavior in the inelastic range, a coefficient of 10 is typically selected. It is important to note that for the 3D buildings with a concrete slab, external walls of 30 cm, internal walls of 11 cm, and a potential shotcrete or coating layer, the order of failure under increasing PGA is as follows: first the internal walls, then the external walls, followed by the retrofitting implementations, and finally the roof slab. This means that to observe greater nonlinearity during loading, the failure of the internal walls is disregarded, and the analysis is halted as soon as the external walls fail.

e. The amount of surcharge on top of the masonry walls

f. The effect of openings in the masonry walls

g. Applying different earthquakes in both the longitudinal and transverse directions of the 3D buildings to investigate the influence of higher modes in the MPA-based IDA

Based on the description in subsection 3, the masonry structure undergoes dynamic analysis to obtain the mode shapes for the first few dominant modes. The entire structure is then subjected to monotonically increasing forces for each mode, generating the pushover curve (base shear versus maximum displacement of the structure). During the pushover analysis, the forces are steadily increased to induce the level of nonlinearity detailed in paragraph (d). Next, the dynamic equation of the main structure is converted into a SDOF system using Equation 15 and is solved to obtain the nonlinear behavior curve from the previous step. Finally, the maximum displacement of the SDOF system is transformed back into the principal MDOF structure using Equation 16.

### 4.5. Results

In the following section, as stated in subsection 4.4, the median results of the IDA and MPA techniques will be presented. A nonlinearity coefficient of 10 and a surcharge of 3000 kg/m³ on the roof of the 3D buildings will be applied unless otherwise specified. Furthermore, in all analyses, except for subsection 4.5.6, only the first mode is considered in the MPA algorithm.

#### 4.5.1. The effect of retrofitting

The three 2D walls (shown in Figure 4) are evaluated for in-plane loadings in the absence of surcharge, considering both unreinforced and retrofitted conditions with shotcrete implementation. The results of the IDA and MPA curves are presented in Figures 8 to 10.

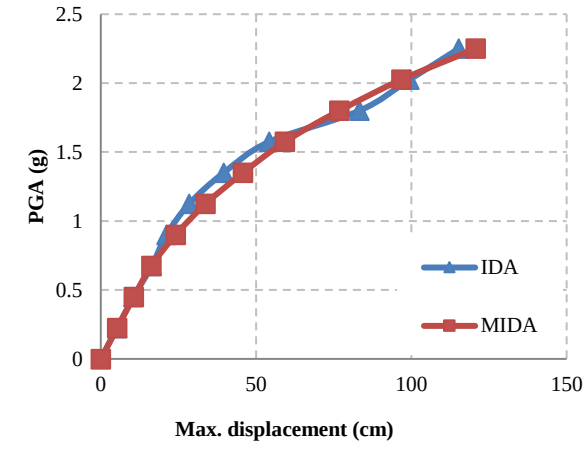


(a)

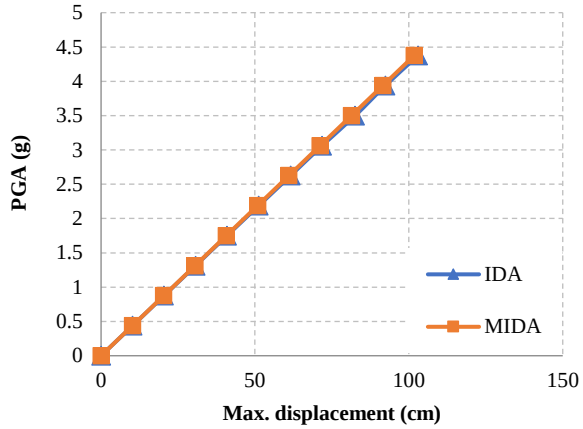


(b)

**Figure 8. Medium IDA and MIDA curves for wall without hole, (a) Unreinforced, (b) Retrofitted**

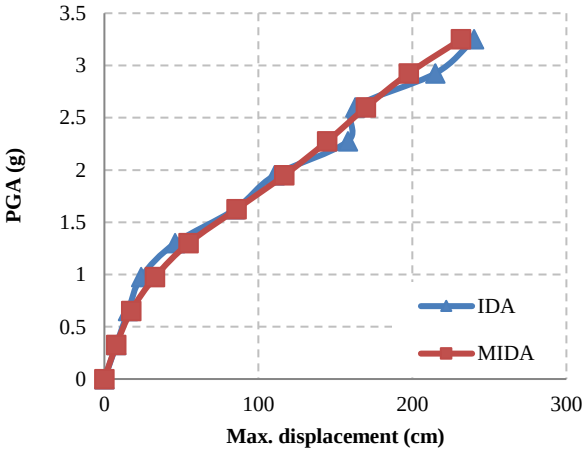


(a)

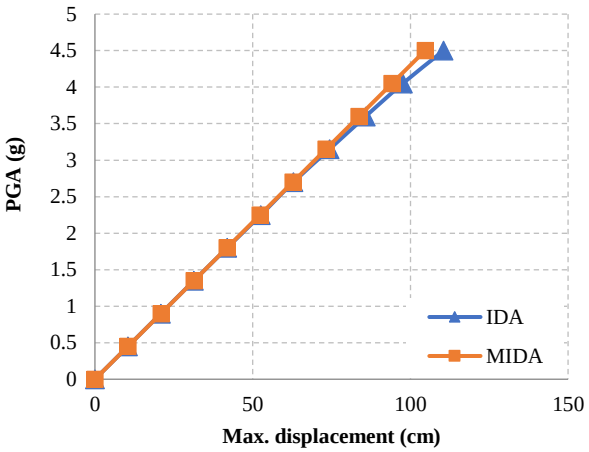


(b)

**Figure 9. Medium IDA and MIDA curves for wall with hole 0.5×0.5 m$^2$, (a) Unreinforced, (b) Retrofitted**

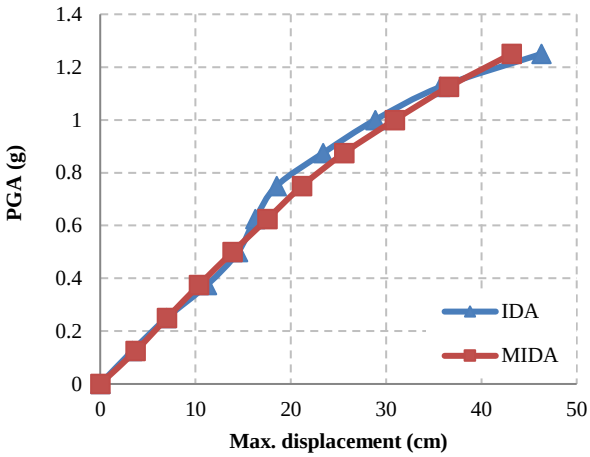


(a)

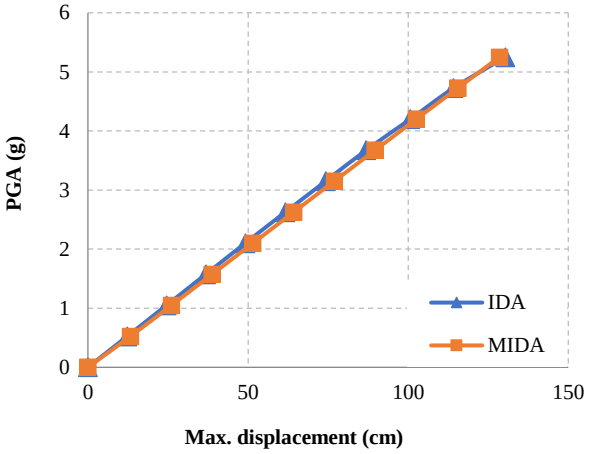


(b)

**Figure 10. Medium IDA and MIDA curves for wall with hole 1×1 m$^2$, (a) Unreinforced, (b) Retrofitted**

In the case of unreinforced walls, greater discrepancies are observed, with a maximum error of less than 16%. In contrast, the error for reinforced walls is below 6%. The differences between the IDA and MPA curves tend to diminish for structures designed to be stronger, and the improvement in reinforced walls can be observed by analyzing the maximum PGA. Consequently, these walls

can withstand more significant loads for the given level of nonlinearity compared to unreinforced walls. Additionally, strength reduction due to the dimensional expansion of openings is evident. In other words, as the opening dimensions increase, either the maximum PGA decreases, or for a similar PGA, the maximum displacement increases, resulting in a smaller ratio of maximum PGA to maximum displacement.

### 4.5.2. The effect of loading direction

The 3D buildings - one-story, two-story, and three-story - are analyzed in both the longitudinal and transverse directions. The corresponding outputs are presented in Figures 11 to 13.

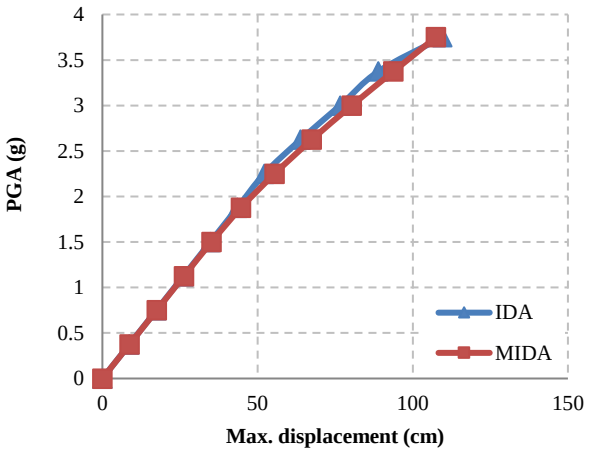


(a)

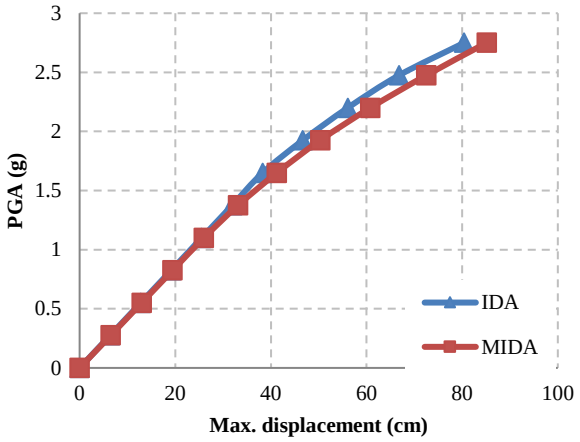


(b)

**Figure 11. Medium IDA and MIDA curves for the one-story building, (a) longitudinal, (b) transverse**

The total area of the walls in the longitudinal direction is 56% greater than that in the transverse direction. Consequently, the longitudinal direction exhibits more resistance than the transverse direction. Additionally, it is observed that the IDA curves for the longitudinal direction show higher maximum PGA values compared to the transverse direction for all one-, two-, and three-story buildings. Furthermore, as the number of stories increases, the maximum PGA decreases in both the longitudinal and transverse directions due to the reduction in overall stiffness of high-rise buildings compared to low-rise buildings. In accordance with the above curves, the maximum errors between the IDA and MPA curves are summarized for all scenarios in Table 4.

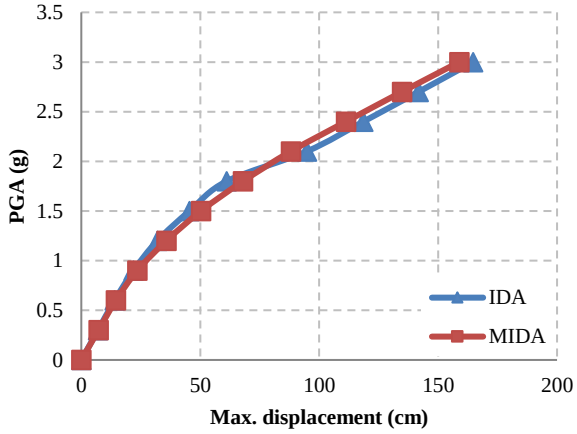


(a)

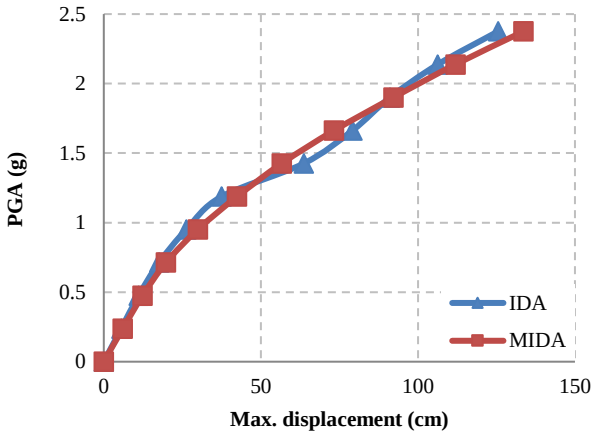


(b)

**Figure 12. Medium IDA and MIDA curves for the two-story building, (a) longitudinal, (b) transverse**

With reference to the above table, as the number of stories increases or as the strengthened longitudinal direction is subjected to loading, the differences between the IDA and MPA techniques decrease. The hypothesis suggests that greater lateral resistance leads to improved consistency between the IDA and MPA algorithms, highlighting a significant finding.

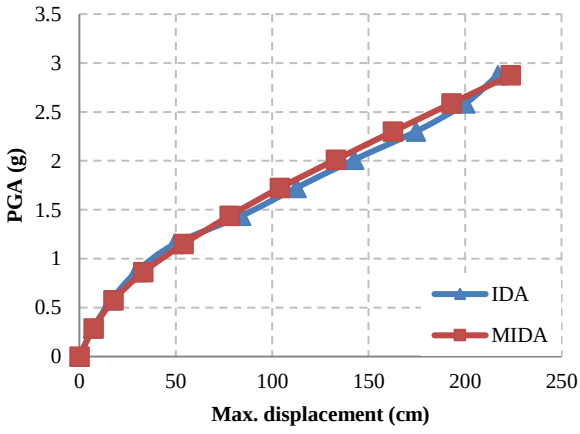


(a)

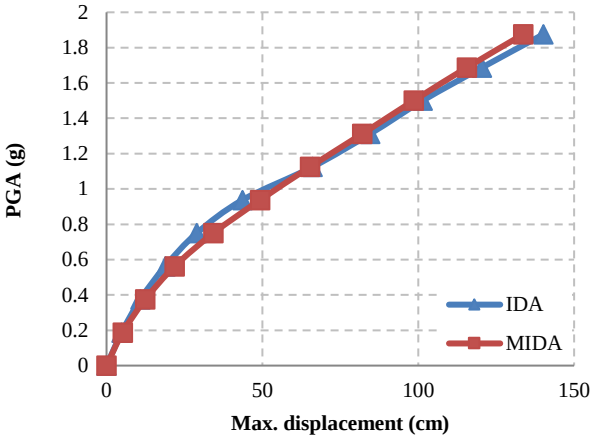


(b)

**Figure 13. Medium IDA and MIDA curves for the three-story building, (a) longitudinal, (b) transverse**

**Table 4. Peak errors from the figures in subsection 4.5.2**

| | One -story | Two-story | Three-story |
|---|---|---|---|
| **Longitudinal dir.** | 6.36% | 11.88% | 12.41% |
| **Transverse dir.** | 8.53% | 13.92% | 18.44% |

### 4.5.3.The effect of story number

The one-story, two-story, and three-story 3D buildings are examined with a nonlinearity coefficient of 1 in the longitudinal direction, and the IDA and MPA results are shown in Figure 14.

It is clear that a lower nonlinearity coefficient results in a smaller maximum PGA, a trend evident when comparing the figures above with previous ones. As previously noted, buildings with more stories tend to be weaker under lateral loading; thus, increased PGA leads to either lower PGA, higher maximum displacement, or a smaller ratio of PGA to maximum displacement. The maximum errors for the one-, two-, and three-story buildings are 2.95%, 11.04%, and 15.63%, respectively, indicating that reduced lateral strength contributes to greater discrepancies between the IDA and MPA curves

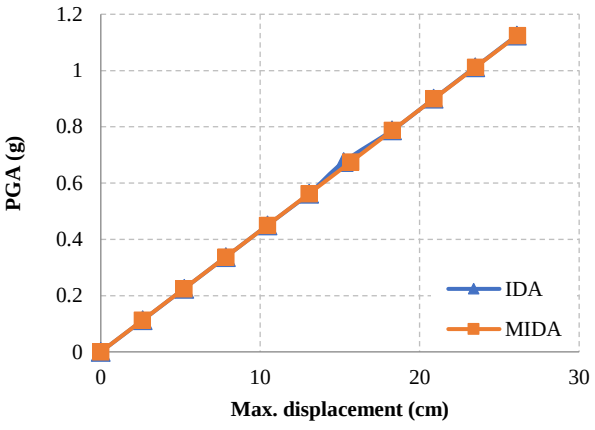


(a)

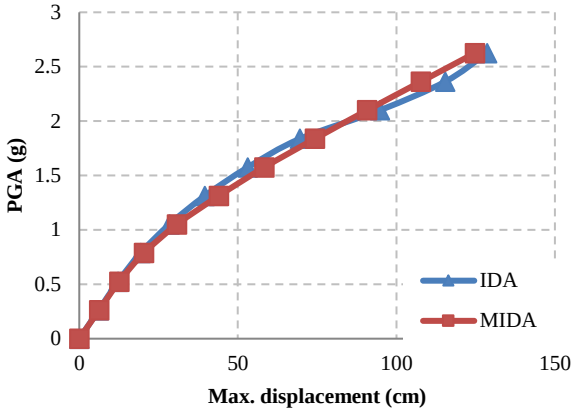


(b)

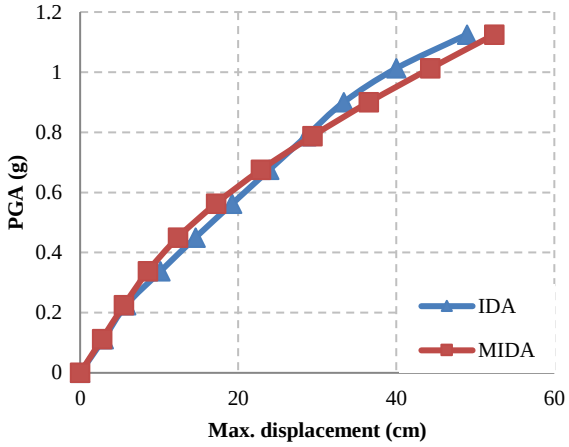


(c)

**Figure 14. Medium IDA and MPA curves: (a) One-story building, (b) Two-story building, (c) Three-story building**

### 4.5.4.The effect of retrofitting methods

The one-story, two-story, and three-story 3D buildings retrofitted with both shotcrete and coating are evaluated in the longitudinal direction. Figures 15 to 17 illustrate the effect of retrofitting methods on the IDA and MPA curves.

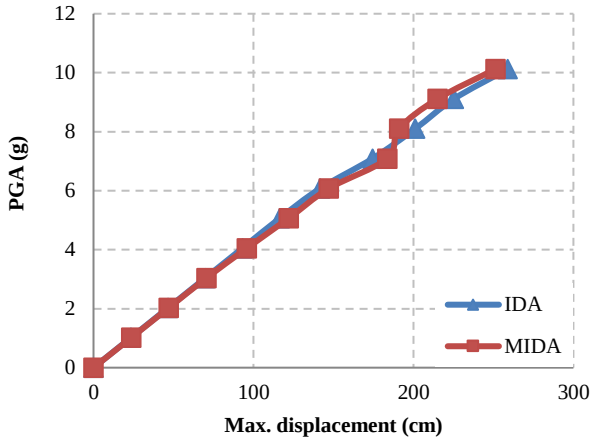


(a)

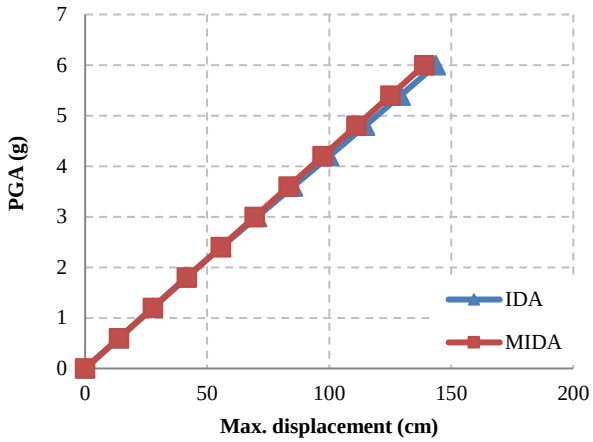


(b)

**Figure 15. Medium IDA and MPA curves for the one-story building: (a) Shotcrete, (b) Coating**

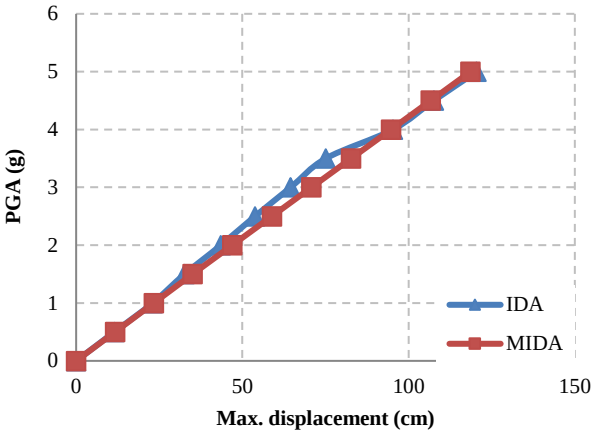


(a)

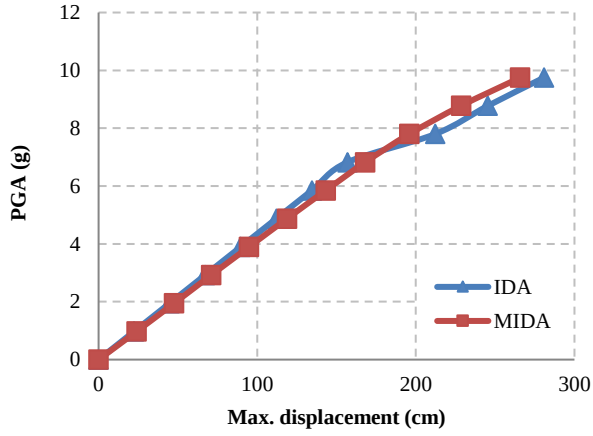


(b)

**Figure 16. Medium IDA and MIDA curves for the two-story building, (a) Shotcrete, (b) Coating**

Comparing the above figures further reinforces that reinforcement leads to IDA and MPA curves exhibiting higher PGA values, even in the elastic range, which is linearly observable in the curves. An increase in the number of stories in reinforced masonry buildings with shotcrete applications results in higher maximum PGA, while the coating application exhibits the opposite behavior. All previously mentioned observations for Figures 11, 12, and 13 apply here as well. In accordance with the above figures, the maximum errors between the IDA and MPA curves are summarized in Table 5.

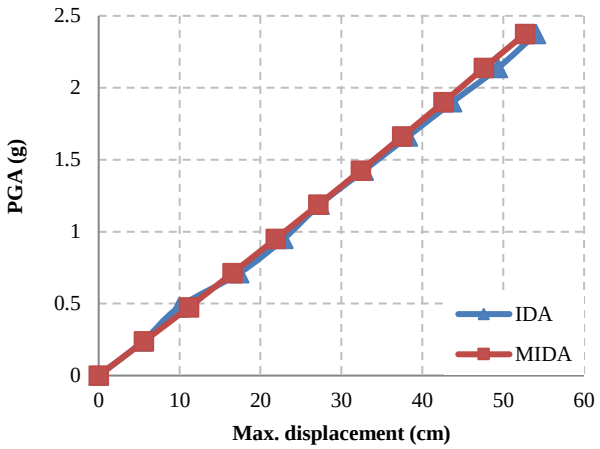


(a)

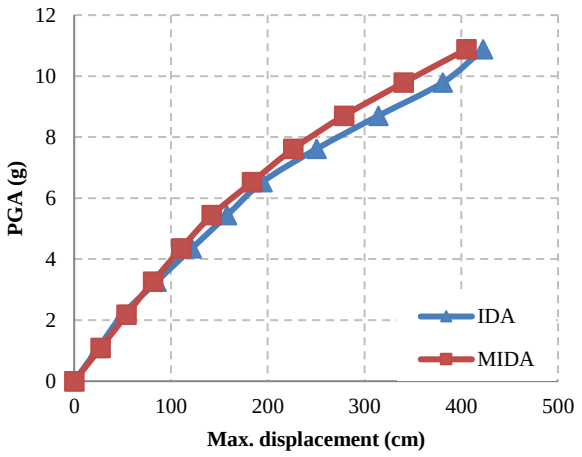


(b)

**Figure 17. Medium IDA and MIDA curves for the three-story building, (a) Shotcrete, (b) Coating**

**Table 5. Peak errors from the figures in subsection 4.5.4**

| | One-story | Two-story | Three-story |
|---|---|---|---|
| **Shotcrete** | 5.31% | 10.15% | 12.39% |
| **Coating** | 3.24% | 7.71% | 11.29% |

Comparing the above figures once again demonstrates that reinforcement leads to IDA and MPA curves exhibiting higher PGA values, even within the elastic range, which is linearly observable in the curves. An increase in the number of stories in reinforced masonry buildings with shotcrete applications results in higher maximum PGA, while the coating application shows the opposite behavior. All previously mentioned observations for Figures 11, 12, and 13 apply here as well. In accordance with the above figures, the maximum errors between the IDA and MPA curves are summarized in the Table 5.

Table 5 again shows that the MPA technique has lower accuracy for high-rise buildings compared to low-rise buildings. Notably, the coating application generally provides better accuracy for the MPA technique, indicating

that it may be more effective despite being less cost-effective than shotcrete application.

### 4.5.5. The effect of surcharge pressure

The 2D wall without a hole is examined in the in-plane direction for different surcharge amounts. Table 6 displays the medium IDA and MPA values corresponding to the various surcharge pressures for the wall without a hole.

**Table 6. Medium IDA and MIDA for the perforated wall**

| | IDA | MIDA | Err. (%) | IDA | MIDA | Err. (%) |
|---|---|---|---|---|---|---|
| **PGA (g)** | **Surcharge = 625 [Pa]** | | | **Surcharge = 1250 [Pa]** | | |
| 0.29 | 6.8 | 6.8 | 0.4 | 6.4 | 7.2 | 12.5 |
| 0.86 | 20.5 | 20.7 | 1.0 | 19.3 | 22.2 | 15.0 |
| 1.44 | 37.2 | 42.0 | 12.9 | 33.6 | 40.7 | 21.1 |
| 2.01 | 73.4 | 72.8 | 0.8 | 58.8 | 72.9 | 24.0 |
| 2.59 | 118.2 | 116.3 | 1.6 | 100.7 | 114.8 | 14.0 |
| **PGA (g)** | **Surcharge = 2500 [Pa]** | | | **Surcharge = 5000 [Pa]** | | |
| 0.28 | 6.5 | 6.7 | 3.1 | 7.2 | 7.0 | 2.2 |
| 0.84 | 19.4 | 20.2 | 4.2 | 21.6 | 21.1 | 2.3 |
| 1.41 | 34.4 | 40.6 | 17.9 | 36.1 | 40.4 | 12.0 |
| 1.97 | 70.5 | 70.5 | 0.1 | 66.6 | 68.5 | 2.9 |
| 2.53 | 130.0 | 111.2 | 14.5 | 121.9 | 105.2 | 13.7 |
| **PGA (g)** | **Surcharge = 10000 [Pa]** | | | **Surcharge = 20000 [Pa]** | | |
| 0.28 | 6.5 | 6.7 | 3.1 | 6.7 | 6.7 | 0.2 |
| 0.84 | 19.4 | 20.2 | 4.2 | 20.0 | 20.2 | 0.9 |
| 1.41 | 37.8 | 40.6 | 7.3 | 36.4 | 40.6 | 11.4 |
| 1.97 | 68.4 | 70.5 | 3.2 | 67.0 | 70.5 | 5.3 |
| 2.53 | 117.5 | 111.2 | 5.3 | 116.1 | 111.2 | 4.3 |
| **PGA (g)** | **Surcharge = 40000 [Pa]** | | | **Surcharge = 80000 [Pa]** | | |
| 0.29 | 6.7 | 6.8 | 1.7 | 8.2 | 6.7 | 18.8 |
| 0.86 | 20.3 | 20.7 | 1.9 | 24.6 | 20.2 | 17.9 |
| 1.44 | 34.9 | 42.0 | 20.4 | 33.5 | 40.6 | 21.3 |
| 2.01 | 74.4 | 72.8 | 2.1 | 121.8 | 70.5 | 42.1 |
| 2.59 | 203.0 | 116.3 | 42.7 | 376.5 | 111.2 | 70.5 |

Although it appears that variations in surcharge do not affect the maximum PGA or MPA outputs, the IDA outputs are remarkably sensitive. In other words, at high surcharge levels, the structures experience instability, leading to significant maximum displacement. Consequently, the maximum errors indicate that MPA results are no longer reliable when additional pressure is applied to the masonry structures.

### 4.5.6. The effects of higher modes

The 3D buildings, one, two and three-story are investigated in both the longitudinal and transverse directions of the buildings so as to investigate higher modes effects on the MIDA analysis. In Tables 7 and 8, the IDA and MIDA results for two-story and three-story buildings are presented:

**Table 7. Medium IDA and MIDA for the two-story building**

| | IDA | MIDA | |
|---|---|---|---|
| | | Mode 1 | Mode 1,2 |
| **PGA (g)** | **Longitudinal direction** | | |
| 0.3 | 7.0 | 7.2 | 7.2 |
| 0.6 | 14.0 | 14.5 | 14.7 |
| 0.9 | 22.0 | 23.5 | 23.7 |
| 1.2 | 32.0 | 35.8 | 35.9 |
| 1.5 | 45.5 | 50.3 | 50.7 |
| 1.8 | 61.1 | 68.0 | 68.3 |
| 2.1 | 94.8 | 88.1 | 88.6 |
| 2.4 | 118.6 | 111.3 | 111.8 |
| 2.7 | 141.8 | 134.8 | 135.4 |
| 3 | 164.7 | 158.9 | 159.4 |
| **PGA (g)** | **Transverse direction** | | |
| 0.2 | 5.5 | 6.0 | 6.3 |
| 0.5 | 11.1 | 12.3 | 12.7 |
| 0.7 | 17.6 | 19.8 | 20.4 |
| 1.0 | 26.2 | 29.9 | 30.5 |
| 1.2 | 37.5 | 42.4 | 43.2 |
| 1.4 | 63.6 | 56.6 | 57.4 |
| 1.7 | 79.1 | 73.3 | 74.2 |
| 1.9 | 91.1 | 92.2 | 93.4 |
| 2.1 | 106.3 | 111.9 | 113.0 |
| 2.4 | 125.5 | 133.6 | 134.8 |

**Table 8. Medium IDA and MIDA for the three-story building**

| | IDA | MIDA | | |
|---|---|---|---|---|
| | | Mode 1 | Mode 1,2 | Mode 1,2,3 |
| **PGA (g)** | **Longitudinal direction** | | | |
| 0.3 | 7.0 | 7.3 | 7.3 | 7.3 |
| 0.6 | 16.5 | 17.7 | 18.6 | 18.6 |
| 0.9 | 29.4 | 33.1 | 34.2 | 34.2 |
| 1.2 | 49.4 | 54.0 | 55.3 | 55.3 |
| 1.4 | 83.9 | 77.9 | 78.9 | 78.9 |
| 1.7 | 112.6 | 104.0 | 105.4 | 105.4 |
| 2.0 | 142.5 | 132.9 | 134.6 | 134.6 |
| 2.3 | 174.5 | 162.6 | 164.7 | 164.8 |
| 2.6 | 200.1 | 192.9 | 194.8 | 194.9 |
| 2.9 | 217.0 | 223.7 | 226.2 | 226.3 |
| **PGA (g)** | **Transverse direction** | | | |
| 0.2 | 4.8 | 5.2 | 5.2 | 5.2 |
| 0.4 | 10.9 | 12.4 | 13.4 | 13.4 |
| 0.6 | 18.8 | 21.9 | 22.9 | 23.0 |
| 0.8 | 29.0 | 34.3 | 35.6 | 35.7 |
| 0.9 | 43.6 | 49.3 | 51.3 | 51.4 |
| 1.1 | 66.1 | 65.3 | 67.3 | 67.5 |
| 1.3 | 84.6 | 82.1 | 84.4 | 84.6 |
| 1.5 | 101.4 | 98.5 | 101.4 | 101.6 |
| 1.7 | 120.5 | 115.6 | 118.7 | 118.9 |
| 1.9 | 140.1 | 133.6 | 136.9 | 137.1 |

The preceding table indicates that considering higher modes in the modal analysis of the MPA technique does not directly impact the error quantities. In some cases, higher modes reduce the maximum discrepancies between the IDA and MPA curves. However, for all conditions, the error variance, which is not significant, may lead to the neglect of higher modes' influence. Furthermore, given the notable reduction in processing time associated with the MPA procedure, this assumption becomes practically advantageous. As shown in Table 9, the effect of higher modes is negligible compared to the primary mode, especially for modes higher than 2. Additionally, it does not matter which direction is subjected to lateral seismic loading. Consequently, it can be concluded that considering the first two modes is generally sufficient in the MPA approach for all masonry buildings.

**Table 9. Maximum displacement (cm) for each mode**

| Step | 2-story building | | 3-story building | | |
|---|---|---|---|---|---|
| | Longitudinal | | | | |
| | Mode 1 | Mode 2 | Mode 1 | Mode 2 | Mode 3 |
| 1 | 7.24 | 0.01 | 7.27 | 0.03 | 0.00 |
| 2 | 14.53 | 0.18 | 17.72 | 0.84 | 0.03 |
| 3 | 23.52 | 0.13 | 33.10 | 1.09 | 0.03 |
| 4 | 35.75 | 0.19 | 54.03 | 1.24 | 0.05 |
| 5 | 50.33 | 0.33 | 77.90 | 0.99 | 0.06 |
| 6 | 67.98 | 0.32 | 104.03 | 1.33 | 0.08 |
| 7 | 88.06 | 0.51 | 132.94 | 1.61 | 0.09 |
| 8 | 111.27 | 0.57 | 162.61 | 2.08 | 0.08 |
| 9 | 134.80 | 0.61 | 192.85 | 1.93 | 0.10 |
| 10 | 158.88 | 0.57 | 223.67 | 2.57 | 0.10 |
| Step | Transverse | | | | |
| | Mode 1 | Mode 2 | Mode 1 | Mode 2 | Mode 3 |
| 1 | 6.04 | 0.26 | 5.19 | 0.03 | 0.01 |
| 2 | 12.34 | 0.33 | 12.44 | 0.97 | 0.03 |
| 3 | 19.79 | 0.64 | 21.88 | 1.05 | 0.09 |
| 4 | 29.90 | 0.64 | 34.29 | 1.33 | 0.06 |
| 5 | 42.41 | 0.83 | 49.27 | 2.01 | 0.11 |
| 6 | 56.60 | 0.83 | 65.30 | 2.05 | 0.11 |
| 7 | 73.30 | 0.95 | 82.09 | 2.36 | 0.18 |
| 8 | 92.17 | 1.23 | 98.52 | 2.87 | 0.18 |
| 9 | 111.93 | 1.07 | 115.61 | 3.12 | 0.19 |
| 10 | 133.62 | 1.22 | 133.65 | 3.22 | 0.21 |

## 5. Conclusions

In the current research, the MPA-based IDA procedure was applied to masonry structures, taking into account various practical parameters, including opening dimensions, story number, surcharge, higher modes, and retrofitting implementations. Ultimately, MPA curves were compared with IDA curves. To summarize, the following highlights some key issues related to the implementation of IDA and MPA curves on masonry buildings:

- Except under large surcharge conditions, the conformity of IDA and MPA curves is reasonable, with the maximum error typically being less than 15%. In conclusion, the MPA technique is reliable, practical, preferable, and significantly faster than the IDA approach while still being accurate.
- For high surcharge conditions, masonry structures are prone to failure, leading to significant discrepancies between MPA and IDA results. Therefore, the use of the MPA algorithm should be avoided in such cases.
- As previously mentioned several times, more vigorous structures under lateral loadings give the best estimation of IDA curves. For convenient accuracy, the error between IDA and MIDA curves can be underestimated. Concerning this matter, elastic ranges are usually becoming longer. Consequently, the MIDA technique provides fewer errors in comparison with the IDA algorithm in the following structures:
  - ✓ Reinforced structures
  - ✓ Structures without openings
  - ✓ Low-rise buildings
- The coating application reinforces buildings more effectively than shotcrete; however, the thickness of the coating significantly influences this preference. Consequently, the coating implementation results in greater conformity between IDA and MPA curves.
- Although considering higher effective modes makes the MPA algorithm very time-consuming, the final results do not vary significantly. Overall, it is highly recommended to use the MPA technique by incorporating only the first two primary modes for all masonry structures.

## 6. References

[1] Vamvatsikos, D., & Cornell, C. A. (2001). Incremental dynamic analysis. Earthquake Engineering & Structural Dynamics, 31(3), 491–514. doi:10.1002/eqe.141.

[2] Park, Y., & Ang, A. H. -S. (1985). Mechanistic Seismic Damage Model for Reinforced Concrete. Journal of Structural Engineering, 111(4), 722–739. doi:10.1061/(asce)0733-9445(1985)111:4(722).

[3] Chopra, A. K., & Goel, R. K. (2002). A modal pushover analysis procedure for estimating seismic demands for buildings. Earthquake Engineering and Structural Dynamics, 31(3), 561–582. doi:10.1002/eqe.144.

[4] Mofid, M., Zarfam, P., & Fard, B. R. (2005). On the modal incremental dynamic analysis. Structural Design of Tall and Special Buildings, 14(4), 315–329. doi:10.1002/tal.271.

[5] Zarfam, P., & Mofid, M. (2011). On the modal incremental dynamic analysis of reinforced concrete structures, using a trilinear idealization model. Engineering Structures, 33(4), 1117–1122. doi:10.1016/j.engstruct.2010.12.029.

[6] Han, S. W., & Chopra, A. K. (2006). Approximate incremental dynamic analysis using the modal pushover

analysis procedure. Earthquake Engineering and Structural Dynamics, 35(15), 1853–1873. doi:10.1002/eqe.605.

[7] Zafarkhah, E., & Dehkordi, M. R. (2017). Extending the modal incremental dynamic analysis method for structures equipped with viscoelastic dampers. Journal of Vibroengineering, 19(2), 783–800. doi:10.21595/jve.2016.17181.

[8] Zarfam, P., & Mofid, M. (2009). Evaluation of modal incremental dynamic analysis, using input energy intensity and modified bilinear curve. Structural Design of Tall and Special Buildings, 18(5), 573–586. doi:10.1002/tal.461.

[9] Xiang, Y., Luo, Y. feng, & Shen, Z. yan. (2017). An extended modal pushover procedure for estimating the in-plane seismic responses of latticed arches. Soil Dynamics and Earthquake Engineering, 93, 42–60. doi:10.1016/j.soildyn.2016.12.005.

[10] Polyakov, S. V. (1960). On the interaction between masonry filler walls and enclosing frame when loaded in the plane of the wall. Translations in earthquake engineering, 2(3), 36-42.

[11] Holmes, M. (1961). Steel Frames With Brickwork and Concrete Infilling. Proceedings of the Institution of Civil Engineers, 19(4), 473–478. doi:10.1680/iicep.1961.11305.

[12] Stafford Smith, B. (1967). Methods for predicting the lateral stiffness and strength of multi-storey infilled frames. Building Science, 2(3), 247–257. doi:10.1016/0007-3628(67)90027-8.

[13] Hetényi, M., & Hetbenyi, M. I. (1946). Beams on elastic foundation: theory with applications in the fields of civil and mechanical engineering. University of Michigan Press, Ann Arbor, United States.

[14] Reflak, J., & Fajfar, P. (1991). Elastic analysis of infilled frames using substructures. Earthquake Engineering, 285–292. doi:10.3138/9781487583217-037.

[15] Hamburger, R. O., & Chakradeo, A. S. (1993). Methodology for seismic capacity evaluation of steel-frame buildings with infill unreinforced masonry. Mitigation and damage to the built environment, Central United States Earthquake Consortium (CUSEC), Memphis, United States.

[16] Skafida, S., Koutas, L., & Bousias, S. N. (2014). Analytical Modeling of Masonry Infilled RC Frames and Verification with Experimental Data. Journal of Structures, 2014, 1–17. doi:10.1155/2014/216549.

[17] Roca, P., Molins, C., & Marí, A. R. (2005). Strength Capacity of Masonry Wall Structures by the Equivalent Frame Method. Journal of Structural Engineering, 131(10), 1601–1610. doi:10.1061/(asce)0733-9445(2005)131:10(1601).

[18] Magenes, G. (2000, January). A method for pushover analysis in seismic assessment of masonry buildings. Proceedings of the12th world conference on earthquake engineering, 30 January-4 February, Auckland, New Zealand.

[19] Lagomarsino, S., Penna, A., Galasco, A., & Cattari, S. (2013). TREMURI program: An equivalent frame model for the nonlinear seismic analysis of masonry buildings. Engineering Structures, 56, 1787–1799. doi:10.1016/j.engstruct.2013.08.002.

[20] Rots, J. G., & Blaauwendraad, J. (1995). Two approaches for the analysis of masonry structures: micro and macro-modeling. Heron, 40(4).

[21] Lourenço, P. B. (1997). Computational strategies for masonry structures. PhD Thesis, Delft University of Technology, Delft, Netherlands.

[22] Lourenço, P. B. (1994). Analysis of masonry structures with interface elements: Theory and applications. Faculteit der Civiele Techniek, TU Delft,, Delft, Netherlands.

[23] Zucchini, A., & Lourenço, P. B. (2004). A coupled homogenisation-damage model for masonry cracking. Computers and Structures, 82(11–12), 917–929. doi:10.1016/j.compstruc.2004.02.020.

[24] Lourenço, P. B. (1997). An anisotropic macro-model for masonry plates and shells: Implementation and validation. Faculty of Civil Engineering, Mechanics and Structures, Computational Mechanics, Delft University of Technology, Delft, Netherlands.

[25] Bhattacharya, S., Nayak, S., & Dutta, S. C. (2014). A critical review of retrofitting methods for unreinforced masonry structures. International Journal of Disaster Risk Reduction, 7, 51–67. doi:10.1016/j.ijdrr.2013.12.004.

[26] Lin, Y. W., Wotherspoon, L., Scott, A., & Ingham, J. M. (2014). In-plane strengthening of clay brick unreinforced masonry wallettes using ECC shotcrete. Engineering Structures, 66, 57–65. doi:10.1016/j.engstruct.2014.01.043.

[27] Khan, H. A., Roy, P., & Nanda, R. P. (2016). Retrofitting of Brick Masonry Panels with Glass Fibre Reinforced Polymers. IOSR Journal of Mechanical and Civil Engineering, 16(053), 11–18. doi:10.9790/1684-16053011118.

[28] Sathiparan, N., Nissanka, N. A. A. C., & Priyankara, R. L. S. (2016). A Comparative Study of Meshtype Retrofitting for Unreinforced Masonry Under In-plane Loading. Arabian Journal for Science and Engineering, 41(4), 1391–1401. doi:10.1007/s13369-015-1937-x.

[29] Moroz, J. G., Lissel, S. L., & Hagel, M. D. (2014). Performance of bamboo reinforced concrete masonry shear walls. Construction and Building Materials, 61, 125–137. doi:10.1016/j.conbuildmat.2014.02.006.

[30] Feo, L., Luciano, R., Misseri, G., & Rovero, L. (2016). Irregular stone masonries: Analysis and strengthening with glass fibre reinforced composites. Composites Part B: Engineering, 92, 84–93. doi:10.1016/j.compositesb.2016.02.038.

[31] Nayak, S., & Dutta, S. C. (2016). Improving Seismic Performance of Masonry Structures with Openings by Polypropylene Bands and L-Shaped Reinforcing Bars. Journal of Performance of Constructed Facilities, 30(2). doi:10.1061/(asce)cf.1943-5509.0000733.

[32] Kalliontzis, D., & Schultz, A. E. (2017). Improved estimation of the reverse-cyclic behavior of fully-grouted masonry shear walls with unbonded post-tensioning. Engineering Structures, 145, 83–96. doi:10.1016/j.engstruct.2017.05.011.

[33] Santandrea, M., Quartarone, G., Carloni, C., & Gu, X. (2017). Confinement of masonry columns with steel and basalt FRCM composites. Key Engineering Materials, 747 KEM, 342–349. doi:10.4028/www.scientific.net/KEM.747.342.

[34] Ismail, N., & Ingham, J. M. (2016). In-plane and out-of-plane testing of unreinforced masonry walls strengthened using polymer textile reinforced mortar. Engineering Structures, 118, 167–177. doi:10.1016/j.engstruct.2016.03.041.

[35] Sathiparan, N., Sakurai, K., Numada, M., & Meguro, K. (2014). Seismic evaluation of earthquake resistance and retrofitting measures for two story masonry houses. Bulletin of Earthquake Engineering, 12(4), 1805–1826. doi:10.1007/s10518-014-9587-z.

[36] Banerjee, S., Nayak, S., & Das, S. (2019). Enhancing the flexural behaviour of masonry wallet using PP band and steel wire mesh. Construction and Building Materials, 194, 179–191. doi:10.1016/j.conbuildmat.2018.11.001.

[37] Messali, F., Metelli, G., & Plizzari, G. (2017). Experimental results on the retrofitting of hollow brick masonry walls with reinforced high performance mortar coatings. Construction and Building Materials, 141, 619–630. doi:10.1016/j.conbuildmat.2017.03.112.

[38] Zienkiewicz, O. C., & Taylor, R. L. (2000). The finite element method: The basis. Butterworth-Heinemann, Oxford, United Kingdom.

[39] Zienkiewicz, O. C., & Taylor, R. L. (2000). The finite element method: solid mechanics. Butterworth-Heinemann, Oxford, United Kingdom.

[40] ASCE/SEI 7-10. (2010). Minimum Design Loads for Buildings and Other Structures. American Society of Civil Engineers (ASCE), Reston, United States. doi:10.1061/9780784412916

[41] Kent, D. C., & Park, R. (1971). Flexural Members with Confined Concrete. Journal of the Structural Division, 97(7), 1969–1990. doi:10.1061/jsdeag.0002957.

[42] Koiter, W. T. (1953). Stress-strain relations, uniqueness and variational theorems for elastic-plastic materials with a singular yield surface. Quarterly of Applied Mathematics, 11(3), 350–354. doi:10.1090/qam/59769.

[43] Page, A. (1981). The Biaxial Compressive Strength of Brick Masonry. Proceedings of the Institution of Civil Engineers, 71(3), 893–906. doi:10.1680/iicep.1981.1825.

[44] Asteris, P. G. (2008). Finite element micro-modeling of infilled frames. Electronic Journal of Structural Engineering, 8, 1–11.

[45] ACI 318-14. (2014). Building Code Requirements for Structural Concrete (ACI 318-14). American Concrete Institute (ACI), Michigan, United States.